# Isotope-Engineering the Thermal Conductivity of Two-Dimensional $MoS_2$

Xufan Li,[†,Δ] Jingjie Zhang,[†,‡,Δ] Alexander A. Puretzky,[†] Anthony Yoshimura,[§] Xiahan Sang,[†] Qiannan Cui,[#] Yuanyuan Li,[#] Liangbo Liang,[†] Avik W. Ghosh,[‡] Hui Zhao,[#] Raymond R. Unocic,[†] Vincent Meunier,[§] Christopher M. Rouleau,[†] Bobby G. Sumpter,[†] David B. Geohegan,[†] Kai Xiao*[,†]

[†]Center for Nanophase Materials Sciences, Oak Ridge National Laboratory, Oak Ridge, Tennessee 37831, USA. [‡]Department of Electrical and Computer Engineering, University of Virginia, Charlottesville, Virginia 22903, USA. [§]Department of Physics, Applied Physics, and Astronomy, Rensselaer Polytechnic Institute, Troy, New York 12180, USA. [#]Department of Physics and Astronomy, University of Kansas, Lawrence, Kansas, 66045, USA.

[Δ]X. Li and J. Zhang contributed equally to this work.

**ABSTRACT**

Isotopes represent a degree of freedom that might be exploited to tune the physical properties of materials while preserving their chemical behaviors. Here we demonstrate that the thermal properties of two-dimensional (2D) transition metal dichalcogenides can be tailored through isotope engineering. Monolayer crystals of $MoS_2$ were synthesized with isotopically-pure $^{100}Mo$ and $^{92}Mo$ by chemical vapor deposition employing isotopically enriched molybdenum oxide precursors. The in-plane thermal conductivity of the $^{100}MoS_2$ monolayers, measured using a non-destructive, optothermal Raman technique, is found to be enhanced by ~50% compared with the $MoS_2$ synthesized using mixed Mo isotopes from naturally occurring molybdenum oxide. The boost of thermal conductivity in isotopically pure $MoS_2$ monolayers is attributed to the combined effects of reduced isotopic disorder and a reduction in defect-related scattering, consistent with observed stronger photoluminescence and longer exciton lifetime. These results shed light on the fundamentals of 2D nanoscale thermal transport important for optimization of 2D electronic devices.

**KEYWORDS:** thermal conductivity, isotope, $MoS_2$, optothermal Raman technique, 2D materials

The emergence of two-dimensional (2D) layered materials, including graphene and beyond, is having an important impact on nanotechnology and quantum information sciences.[1,2] Most notably, semiconducting 2D materials such as the transition metal dichalcogenides (TMDs) break the limitations of their conventional bulk counterparts to provide great variations in electronic structures,[3] electron spin and pseudospin transport,[4,5] many-body effects,[6] and light-matter interactions[7] that could potentially enable many applications in electronics, optoelectronics, and photonics. For these applications, it is also extremely important to understand and tune their thermal transport properties, which directly impact the energy consumption and thermal management of electronic and optoelectronic devices.[8] Their layered structure, with a combination of covalent intra-layer bonds and van der Waals (vdW) inter-layer interactions, naturally results in many interesting physical properties, such as higher in-plane and lower out-of-plane thermal conductivities.[9] For example, monolayer graphene has extremely high in-plane thermal conductivity values (~5000 W/mK), which is promising for heat dissipation in nanoelectronics.[10–13] As 2D TMDs are also now important building blocks in many electronic and optoelectronic systems, finding effective ways to tune and enhance their thermal conductivity is highly desirable.

Isotopes of a given element, as is well known, have identical numbers of protons but differ in the number of neutrons in the nuclei. In crystalline solids, the resulting variation in nuclear mass most directly influences the fundamental phonon frequencies that generally govern the thermal, elastic, and vibrational properties.[14,15] Isotopic variations have also been shown to influence electronic properties, such as electronic band structures and exciton binding energies, due to electron-phonon interactions.[14,15] In addition, spin-dependent properties relevant to quantum information science can also be affected *via* electron-nuclear spin interactions when electronic excitations are coupled to long-lived nuclear spin states that have variations in nuclear spin

numbers due to different isotopes.[16–18] Therefore, isotopic effects represent an important, though largely untapped, degree of freedom in 2D materials composition that might be exploited to tune their physical properties while retaining nearly identical chemical behaviors. Such an effect is expected to be even more important in nanomaterials due to their lower dimensions and strong size effects.

It has been predicted and experimentally proven that the thermal properties of 2D crystals can be greatly influenced by isotopes[19,20] due to the substantially different phonon transport properties in 2D system compared to bulk crystals.[21, 22] Recently, isotopically purified graphene with $^{13}C$ has been reported,[19] where adjusting the concentration of $^{13}C$ (from pure $^{12}C$ to mixtures to pure $^{13}C$) showed significant changes in the thermal conductivity, representing the first work on tuning the phonon-related properties of 2D materials through adjustment of isotopic purity. Although theoretical studies have predicted that isotopically enriched $MoS_2$ monolayers should have increased thermal conductivity compared to mixed-isotope monolayers,[20] such tunability of the thermal properties of 2D TMDs through isotope-engineering has yet to be shown experimentally. Therefore, it is important to establish both an experimental demonstration and more detailed theoretical simulation to validate and understand isotope effects on the thermal properties of 2D semiconductors.

There are seven stable naturally occurring isotopes of Mo with atomic masses of 92, 94, 95, 96, 97, 98, and 100, with relative abundances of 14.65%, 9.19%, 15.87%, 16.67%, 9.58%, 24.29%, and 9.74%, respectively. Naturally abundant Mo has an average atomic mass of ~96. In TMDs like $MoS_2$ and $WS_2$, the isotopes of metal atoms generally have a larger impact on the thermal conductivity than the chalcogen isotopes. This is because Mo or W are heavier than S, and contribute more to the eigenvectors of low-frequency acoustic phonon modes. For example, S

isotopes can influence optical phonons from 8–14 THz while Mo isotopes impact acoustic phonons in the frequency range of 2−7 THz that dominate thermal transport at room temperature.[16]

In this work, we demonstrate that the thermal conductivities of TMD monolayers can be tailored through isotopic engineering. Natural ($^{Nat}MoS_2$, schematically depicted in **Figure 1**a), $^{92}Mo$ ($^{92}MoS_2$, 98% enrichment), and $^{100}Mo$ ($^{100}MoS_2$, 98% enrichment) enriched–$MoS_2$ monolayers were grown using CVD. The in-plane thermal conductivity of $^{100}MoS_2$ monolayers, measured using a non-destructive, optothermal Raman technique, is increased by ~50% compared with those containing naturally-abundant Mo. First-principles calculations indicate that the enhanced thermal conductivity in isotopically pure $MoS_2$ monolayers is principally due to the reduced isotope scattering of phonons. In addition, Mo-isotopically pure monolayers are also less defective as indicated by enhanced photoluminescence (PL) and exciton lifetime.

## RESULTS AND DISCUSSION

Monolayer $MoS_2$ crystals were grown on silicon substrates with 250 nm $SiO_2$ using a CVD method similar to that described in previous reports,[23] in which $MoO_3$ was reduced by vaporized sulfur at 700 ºC under ambient pressure. In our experiments, we used natural $MoO_3$ (Alfa Aesar, 99.95%) and isotopically enriched $MoO_3$ (*e.g.*, $^{92}MoO_3$ and $^{100}MoO_3$ with 98% enrichment obtained from Trace Sciences International Corp., 99.70%) to grow $MoS_2$ monolayer crystals with the corresponding isotopic compositions (see Methods Section for details). The growth conditions for all $MoS_2$ samples were the same, which resulted in similar large, triangular monolayer crystals (edge lengths up to hundreds of micrometers with uniform thickness ~0.65 nm), as shown in Figure 1 b, c and Figure S1. Z-contrast high-angle annular dark field scanning transmission electron microscopy (HAADF-STEM) revealed the atomic structure of monolayer $MoS_2$, which appears in plane view as honeycombed hexagonal rings with alternate Mo and S sites (Figure 1c and Figure

S2). The regularity of the hexagonal structure indicates good crystallinity of the as-synthesized $MoS_2$ monolayers. It is difficult to distinguish different isotopes in the HAADF-STEM image (Figure S2) because Mo isotope atoms show very similar contrast in HAADF-STEM images due to the same electron scattering cross-sections resulting from their similar electronic structure and electron density (although different atomic mass can lead to different Debye Waller factors, the influence on scattering intensity is negligible).

The quality and uniformity of the $MoS_2$ monolayers was further examined using PL spectroscopy. PL mapping (**Figure 2**a) of the integrated PL band intensities (as in Figure 2b) was generally uniform across the different flakes, indicating good crystalline quality, except for the enhanced intensity at the crystal edges (Figure 2a) which can be caused by several factors including the dielectric environment, adsorbates, or defects.[24] The observed PL bands are typical for $MoS_2$ monolayers on $SiO_2$ substrates (Figure 2b), with slight shifts (~ 15 meV) observed as the average nuclear mass of Mo increases in the $MoS_2$ monolayers. Contributions to such band shifts can result both from the electronic bandgap difference resulting from the change of volume with isotopic mass, and from differences in substrate-induced strain that occur during growth.[14] It is also systematically observed that the isotopically purified monolayers show higher PL intensity than the natural ones. We attribute this to the longer exciton lifetime observed in femtosecond transient absorption spectroscopy (TAS) of $^{Nat}MoS_2$ and $^{100}MoS_2$ monolayers performed in reflection geometry (Figure 2c). The initial fast decay in the TAS of both samples is ~1 ps, which can be assigned to formation of excitons from the injected free carriers, and followed by a single exponential decay that can be assigned to the exciton lifetime, which are 30 (± 9) and 82 (± 14) ps for $^{Nat}MoS_2$ and $^{100}MoS_2$, respectively. The measured lifetimes are limited by nonradiative recombination of excitons, which is often dominated by defects. Hence, the longer exciton lifetime in the isotopically purified sample suggests a lower defect density.

Raman scattering is one of the most effective method to investigate the vibrational properties in isotopically pure materials due to the mass effect on vibrational frequencies. **Figure 3**a shows the Raman spectra of $^{Nat}MoS_2$, $^{92}MoS_2$, and $^{100}MoS_2$ monolayers, featuring the typical $E^1_{2g}$ and $A_{1g}$ vibrational modes of $MoS_2$. Due to isotopic effects, the in-plane $E^1_{2g}$ mode, in which the vibration of Mo is involved,[25,26] is down shifted from 385.7 $cm^{-1}$ to 382.6 $cm^{-1}$, and then to 380.7 $cm^{-1}$ as the nuclear mass of Mo in $MoS_2$ monolayers increases from 92 to ~96 (average mass of natural Mo), and then to 100. Such a red shift is consistent with results from first-principles calculations (calculation details are in Supporting Information), as shown in Table 1, although the calculated frequencies are slightly larger due to the over binding tendency (*i.e.*, leading to larger force constants) of the local density approximation (LDA) functional used in the density functional theory calculations.[25,27] The frequency decrease of the $E^1_{2g}$ mode with the increased nuclear mass of Mo is expected, as oscillators of greater mass typically vibrate with a smaller frequency. In contrast, the $A_{1g}$ mode is essentially independent of the nuclear mass of Mo in the three $MoS_2$ monolayers. This can be explained by the fact Mo is not involved in this out-of-plane vibration,[25,26] as confirmed by the theoretical calculations (Table 1) that show minute frequency changes of the $A_{1g}$ mode for different isotopes. It is also interesting to note that a weak and broad peak is present at ~450 $cm^{-1}$ in the Raman spectrum of $^{Nat}MoS_2$ monolayer (see Figure 3b for enlarged view), which has been assigned in the literature to the 2LA(M) mode, a second order peak caused by a double resonance effect involving two LA(M) phonons.[28,29] As expected, since the frequency of the 2LA(M) mode is twice that of the LA(M) phonon, its peak shift induced by the Mo isotope is roughly double that of the $E^1_{2g}$ mode, as shown in Figure 3 and Table 1. In addition, the bilayer $MoS_2$ with AB and AA' stacking show similar shifts of the Raman vibrational modes by the Mo isotope (Figure S3), which is also validated by the calculations (Table S1).

In order to understand the isotope effect of $MoS_2$ monolayers on their in-plane thermal conductivity, we used the $^{Nat}MoS_2$, the isotopically pure $^{100}MoS_2$, as well as a monolayer partially enriched by $^{100}Mo$ (*i.e.*, synthesized using a mixture of 1:1 $^{100}MoO_3$ and $^{Nat}MoO_3$, denoted as 50% $^{100}MoS_2$). The thermal conductivity was measured using an optothermal Raman technique similar to those previously used for graphene and TMD layers.[30–32] To conduct these measurements, it is important to eliminate any substrate from underneath the 2D crystals as it might affect the flow of heat. Consequently, the as-grown $^{Nat}MoS_2$, $^{100}MoS_2$, and 50% $^{100}MoS_2$ monolayers were transferred onto a 50 nm-thick porous $Si_3N_4$ film (~2 μm pore size) supported by a Si TEM grid (**Figure 4**a). The transferred monolayers have alternating suspended and $Si_3N_4$-supported regions, and a focused laser (532 nm) was used to measure the Raman spectra with different laser powers and at different temperatures in both regions (Figure 4b). It was observed that, within the environmental temperature range (~290−470 K) and the laser power range (~15−150 μW), the Raman modes of all the $MoS_2$ monolayers shift linearly towards lower frequencies in response to either increasing environment temperature (Figure 4c and Figure S4) or increasing laser power (Figure 4d and Figure S5), which both result in heating the monolayers. The nonlinearity of the Raman mode shift is not considered here since it only matters at higher temperatures [33,34] or larger laser power (> 0.25mW).[31] The slope of the linear curves in Figure 4c, d is the temperature-coefficient ($\chi_T$) and power-coefficient ($\chi_P$) of the $A_{1g}$ mode for suspended $MoS_2$ monolayers (the values are shown Table 2). The $MoS_2$ monolayer that is more isotopically enriched shows a smaller $\chi_P$ and larger $\chi_T$ values, and thus a lower thermal resistance ($R_m = \chi_P/\chi_T$) (Figure 4c, d and Table 2), suggesting the highest in-plane thermal conductivity in $^{100}MoS_2$ monolayers followed by the 50% $^{100}MoS_2$, and $^{Nat}MoS_2$. The $R_m$ is also equal to the measured temperature *versus* total absorbed laser power ($T_m/P$), which was subsequently used to calculate the values of thermal conductivity of the $MoS_2$ monolayers based on the equations established in previous reports[30–32] (see Supporting

Information for the detailed calculations). As a result, the in-plane thermal conductivity ($\kappa_{sus}$) of the suspended $^{100}MoS_2$ and 50% $^{100}MoS_2$ monolayers are 61.6 ± 6.0 W/mK and 52.8 ± 2.4 W/mK, respectively, showing a ~50% and a ~30% enhancement compared with the $^{Nat}MoS_2$ (40.8 ± 0.8 W/mK). Both of these values may be underestimated due to the assumption that all phonon modes by Raman thermal measurement are in equilibrium. However, the reduced thermal resistance $R_m$ in enriched $MoS_2$ indicates that the enhancement should not be underestimated. The results demonstrate that the in-plane thermal conductivity is enhanced in the crystals containing pure Mo isotopes, which could be due to the reduction of phonon scattering.

In the thermal conductivity calculation, we used the temperature- and power-dependence of $A_{1g}$ mode because it is insensitive to the in-plane strain, which includes no significant influence on its Raman frequency from the substrate. The temperature- and power-dependence of $E^1_{2g}$ mode are also shown in Figure S6. Note that the $A_{1g}$ mode is independent of the mass of Mo isotopes under only the harmonic approximation (Figure 3 and Table 1), but it is strongly sensitive to the local temperature variations due to thermal expansion. Therefore, it can be used as a direct measurement for the thermal conductivity. To determine $\kappa_{sus}$ using our calculations, we also need to measure $\chi_T$ and $\chi_P$ in the monolayer region supported by the $Si_3N_4$ film (Figure S7). Note that the $R_m$ ($\chi_P/\chi_T$) of supported $MoS_2$ monolayers includes a relationship between $g$ (the interfacial thermal conductance between the monolayers and $Si_3N_4$) and $\kappa_{sup}$ (in-plane thermal conductivity in the supported monolayers), which is needed in the calculation of $\kappa_{sus}$ (see detailed calculation methods). As shown in Table 2, the $R_m$ values for the supported $^{Nat}MoS_2$ and $^{100}MoS_2$ monolayer under the same external conditions are almost the same, which means that if the interfacial thermal conductance is insensitive to the Mo isotopes in the $MoS_2$ monolayers, $\kappa_{sup}$ of $^{Nat}MoS_2$ and $^{100}MoS_2$ monolayer are similar. Within a reasonable range of $\kappa_{sup}$ from 24.3 to 110 W/mK for monolayer $MoS_2$ supported by $Si_3N_4$ film,[31] the $g$ value only varies from 14.26 to 12.06 MW/m$^2$K (Figure

S8a). By solving the radial heat diffusion equation using these $g$ and $\kappa_{sup}$ values (see detailed calculation methods), $\kappa_{sus}$ of the $MoS_2$ monolayers varies only by less than 3% (*i.e.*, from 40.0 to 40.8 W/mK for $^{Nat}MoS_2$ and from 60.8 to 62.4 W/mK for $^{100}MoS_2$). This also indicates that the local temperature distribution in the $MoS_2$ monolayers is independent of the interfacial thermal conductance, as shown in Figure S8b. This phenomenon is consistent with a previous report on monolayer $MoS_2$ supported by $Si_3N_4$ film.[31]

The thermal conductivity change induced by isotopic compositions in $MoS_2$ monolayers can be caused by the following mechanisms: harmonic property-related mechanisms including the frequency spectrum and the number of modes (*i.e.*, conducting channels) difference, and scattering-based mechanisms including phonon-phonon scattering and isotope scattering.[35] To find the dominant mechanism, we first used the Non-Equilibrium Green's Functions (NEGF) with first-principles parameters to obtain the number of modes in Mo-isotopically pure $^{92}MoS_2$, $^{96}MoS_2$, and $^{100}MoS_2$ monolayers (Figure S9a). The number of modes shows trivial differences as a result of the mass difference of Mo. Since the ballistic thermal conductivity can be expressed as the sum of all the conducting modes over the whole frequency spectrum (see Eq. S7 in Supporting Information), the ballistic thermal conductivity should also show a small difference due to the mass difference of the isotopes.

Next, we calculated the in-plane thermal conductivity of the $^{92}MoS_2$, $^{96}MoS_2$, $^{100}MoS_2$ and $^{Nat}MoS_2$ monolayers using self-consistent Boltzmann Transport Equations (BTE) by considering scattering mechanisms.[36] Convergence is achieved when the relative change in thermal conductivity is less than $10^{-5}$. The self-consistent calculations, beyond the relaxation time approximation, are performed to make sure the scattering processes only take into account the backscattering phonons. Phonon-phonon scattering is included for $^{92}MoS_2$, $^{96}MoS_2$, and $^{100}MoS_2$ monolayers, while extra isotopic scattering is included in calculating the thermal conductivity of

the $^{Nat}MoS_2$ monolayer. The boundary scattering, or the classic size effect[37], is considered by comparing the mean-free-path (MFP) $\lambda$ *versus* the sample sizes $L$ in the Landauer equation (Eq. S4 in Supporting Information). The sample sizes are varied within 1–6 μm to reproduce the experimental samples. This method can cover the transport regimes from the ballistic regime, when the MFP is much larger than the sample size (transmission $\bar{T} = \frac{\lambda}{\lambda+L} \approx 1, \lambda \gg L$), to the diffusive regime when the MFP is much smaller than the sample sizes (transmission $\bar{T} = \frac{\lambda}{\lambda+L} \approx \frac{\lambda}{L}, \lambda \ll L$). Our results are shown in **Figure 5**. The in-plane thermal conductivities of the Mo-isotopically pure $^{92}MoS_2$, $^{96}MoS_2$, and $^{100}MoS_2$ monolayers do not show significant differences (Figure 5, blue, green, and red lines), which are ~100 W/mK at 1 μm, similar to the experimental condition (1 μm radius of suspended monolayers). The result suggests that the small mass difference in isotopes does not lead to enough changes in dispersion or phase space that can significantly affect the phonon-phonon scattering. Unlike the phonon-phonon scattering, once the multiple Mo masses as in the natural $MoS_2$ are considered, the thermal conductivity (Figure 5, black curve) is significantly reduced (87.81 W/mK at 1 μm length) compared to those Mo-isotopically enriched ones. This is because the mass deviation from the average mass by the Mo isotopes is a perturbation that induces a scattering mechanism into the materials[35], referred to as isotope scattering, which greatly shortens the phonon lifetime $\tau$ (Figure S9b) and MFP, and hence reduces the thermal conductivity. The MFP is expressed as $\lambda = \frac{2\langle \tau \cdot v^2 \rangle}{\langle |v| \rangle}$, in which $v$ is the phonon velocity. The phonon lifetime which considers the phonon-phonon scattering and isotopic scattering is obtained using the Matthiessen's rule by summing over the scattering rates: $\frac{1}{\tau} = \frac{1}{\tau_{ph-ph}} + \frac{1}{\tau_{iso}}$. The strength of the isotopic scattering rates $\frac{1}{\tau_{iso}}$ is in the same order of magnitude as the phonon-phonon scattering rates $\frac{1}{\tau_{ph-ph}}$ at 300 K for phonons with wavenumber larger than 150 $cm^{-1}$ as shown in Figure S9b, hence

greatly reducing the lifetime and MFP for those phonons. Based on the above analyses, the increased thermal conductivity in the Mo-isotopically pure $MoS_2$ monolayers is attributed to the reduced isotope scattering (see Supporting Information for first-principles calculation details).

It should be noted that since the presence of defects is not taken into consideration in the calculations presented above, the calculated thermal conductivity values of $MoS_2$ monolayers are higher than those measured experimentally in CVD-grown samples (Table 2). Imperfections in the 2D crystals generally lead to phonon-defect/boundary scattering and thus reducing the thermal conductivity.[6,39] Additional calculations introduced with S vacancies showed that with ~0.4% of S vacancies in the lattice, which is close to the level with typical CVD-grown $MoS_2$ monolayers, the calculated thermal conductivity is consistent with the measured value (Figure S10). In addition, the PMMA residues on the monolayers resulting from the transfer process could also cause a decrease of thermal conductivity.[40] Moreover, the extent of increase of the thermal conductivity in the isotopically pure monolayers (*i.e.*, $^{100}MoS_2$) is found to be larger in experiment (~50%) than in the first-principle calculation (~15%). This suggests that besides reduced isotope scattering, the isotopically pure $MoS_2$ monolayers have less defect-induced phonon scattering, which is also consistent with the observed stronger PL and longer exciton lifetime (Figure 2).

## CONCLUSIONS

In summary, through the chemical vapor deposition synthesis of $MoS_2$ monolayers using isotopically enriched precursors we have demonstrated that isotope engineering can significantly affect several key properties. Optothermal Raman measurements revealed that the in-plane thermal conductivity of isotopically pure $^{100}MoS_2$ monolayers is 50% higher than that those synthesized from naturally abundant isotope mixtures. First-principles lattice dynamics calculations were performed to understand how the isotopic purity enhances thermal conductivity in $MoS_2$

monolayers and concluded that the dominant effect was a reduced isotope mass effect in phonon scattering instead of isotope-induced phonon-phonon scattering. The calculations also predict a higher thermal conductivity for isotopically-pure, defect-free $MoS_2$ monolayers than was experimentally measured, indicating that additional mechanisms should be involved. On the basis of the experimental measurements of enhanced photoluminescence and longer exciton lifetimes for the isotopically-pure samples, we conclude that our more isotopically-pure $MoS_2$ monolayers have fewer defects, further enhancing the thermal conductivity *via* reduced phonon-defect scattering. Overall, the results of our work demonstrate that isotope engineering can effectively tune the thermal conductivity of 2D TMDs. This outcome is important for thermal properties development and thermal management in 2D electronic and optoelectronic building blocks. Given the great potential in tuning the optical, electrical, thermal, and spin properties, isotope engineering in 2D semiconductors could be a promising strategy for 2D electronics, photonics, spin- and valley-tronics, thermoelectricity, and quantum information sciences.

## METHODS

**Materials synthesis.** The natural and isotopically pure $MoS_2$ monolayers were synthesized through a CVD method conducted in a tube furnace system equipped with a 2" quartz tube. In a typical run, the growth substrates, *e.g.*, Si with 250 nm $SiO_2$ ($SiO_2$/Si) substrates cleaned by acetone and isopropanol (IPA) and coated with perylene-3,4,9,10-tetracarboxylic acid tetrapotassium salt (PTAS) as the growth seed, were placed face-down above an alumina crucible containing ~0.5 mg of $MoO_3$ powder, which was then inserted into the center of the quartz tube. Another crucible containing ~0.3 g of S powder was located at the upstream side of the tube. After evacuating the tube to ~5 $\times 10^{-3}$ Torr, the reaction chamber pressure was increased to ambient

pressure through 500 sccm (standard cubic centimeter per minute) argon flow. Then, the reaction was conducted at 700 ºC (with a ramping rate of 40 ºC/min) for 5 min with 80 sccm argon flow. At 700 ºC in the center of the quartz tube, the temperature at the location of S powder was ~200 ºC. After growth, the furnace was allowed to cool naturally to room temperature.

**Monolayer transfer and structural characterization.** The samples for STEM characterization and optothermal Raman-based thermal conductivity measurement were prepared using a wet transfer process. Poly(methyl methacrylate) (PMMA) was first spun onto the $SiO_2$/Si substrate with monolayer crystals at 3500 rpm (revolutions per minute) for 60 s. The PMMA-coated substrate was then floated on 1 M KOH solution, which etched the silica epi-layer, leaving the PMMA film with the monolayer crystals floating on the solution surface. The film was then transferred to deionized water for several times to remove residual KOH. The washed film was scooped onto a 50 nm-thick porous SiN film (~2 μm pore size) supported by a Si TEM grid. PMMA was then removed using acetone and the samples were then soaked in methanol for 12 h to get a clean flake surface. The transferred samples were finally annealed at 300 ºC to get rid of the solvent. STEM images were acquired at 60 kV using a Nion UltraSTEM equipped with a probe aberration corrector (the convergence angle was 31 mrad). The inner and outer collection angle of the HAADF detector were 86 mrad and 200 mrad, respectively. To enhance the signal to noise ratio, atomic resolution STEM images were blurred using a 2D Gaussian distribution.

**PL measurement.** The PL spectra were measured in a custom-built micro-PL/Raman setup. The PL was excited with a continuous wave (cw) diode-pumped solid-state laser (Excelsior, Spectra Physics, 532 nm, 100 mW) through an upright microscope using a 100x-long working distance objective with NA (numeric aperture) = 0.5 (beam radius: ~0.2 μm, FWHM). The typical incident laser power on a sample was maintained at ~3.5 μW to reduce possible laser heating of the samples during PL spectra acquisition. The PL light was analyzed by a spectrometer (Spectra Pro 2300i,

Acton, $f$ = 0.3 m) that was coupled to the microscope with 150 groves/mm grating and a CCD camera (Pixis 256BR, Princeton Instruments). The typical acquisition times were varied from 0.5 to 20 s depending on the PL intensity. The PL mapping was performed using a 0.5 μm steps.

**Femtosecond transient absorption spectroscopy.** In transient absorption measurements, the output of a Ti-sapphire laser, with a central wavelength of 776 nm, a temporal width of about 100 fs, and a repetition rate of about 80 MHz, is divided to two parts by using a beam splitter. One part is used as the pump pulse of 388 nm. The rest of the 776-nm pulse is used to synchronically pump an optical parametric oscillator. The pump and probe pulses are combined by a beam splitter and focused to the sample collinearly with a microscope objective lens. The size of the pump and probe laser spots is ~1.2 μm. The pump fluence and intensity are 1.0 μJ $cm^{-2}$ and 2.2 kHz for all the measurements. This setup allows us to measure the relative change of the probe reflection induced by the pump-injected carriers, $\Delta R/R_0=(R-R_0)/R_0$, where R and $R_0$ are the probe reflection with and without the presence of the pump. This quantity was measured as a function of the probe delay, defined as the delay of the arrival time of the probe pulse at the sample relative to the arrival time of the pump pulse. The probe delay is varied by change the length the probe pulse travels.

**Thermal conductivity measurement.** The laser power-dependent and temperature-dependent Raman spectra of the suspended and $Si_3N_4$-supported $MoS_2$ monolayers were measured in a home-built micro-PL/Raman setup with similar configuration as for PL measurement except for an 1800 groves/mm grating. The power-dependent spectra were acquired at room temperature with the laser power ranging from ~15 to 150 μW, while the temperature-dependent were measured in a home-made stage with in the temperature range of 290−470 K. The calculation of $\kappa_{sus}$ follows closely the established method described in ref 30. This method is based on solving the heat diffusion equation in the cylindrical coordinates:

$$\frac{1}{r}\frac{d}{dr}\left(r\frac{d\mathbf{T}}{dr}\right)+\frac{q'''}{\kappa_{sus}}=0, \qquad (r \le \mathbf{R}) \tag{S1}$$

$$\frac{1}{r}\frac{d}{dr}\left(r\frac{d\mathbf{T}}{dr}\right)-\frac{g}{\kappa_{sup}t}(\mathbf{T}-\mathbf{T_a})+\frac{q'''}{\kappa_{sup}}=0, \qquad (r \ge \mathbf{R}) \tag{S2}$$

, in which $\kappa_{sup}$ is the bassel thermal conductivity in the supported $MoS_2$, $g$ is the interfacial thermal conductance between the $MoS_2$ monolayer and $Si_3N_4$ substrate, $\mathbf{T_a}$ is the environment temperature, $t$ is the thickness of monolayer $MoS_2$ (0.65 nm), $\mathbf{R}$ is the hole radius of the suspended region (1 μm), $q'''$ is the volumetric optical heating expressed as:

$$q''' = \frac{I\alpha}{t}exp(-r^2/r_0^2) \tag{S3}$$

, in which $\alpha$ is the absorbance of the monolayer $MoS_2$ (9% based on ref [31] since we share the same $Si_3N_4$ substrate), $r_0$ is the radius of laser beam size (0.2 μm), $I = P/(\pi r_0^2)$ is the peak laser power per unit area at the center of the beam. The relation between $g$ and $\kappa_{sup}$ was obtained using converged solution for equation 8 in ref [29].

*Conflict of Interest:* The authors declare no competing financial interest.

*Supporting Information Available*: Supporting figures and tables; DFT phonon calculations; thermal conductivity calculations; and vacancy scattering calculations. This material is available free of charge *via* the Internet at http://pubs.acs.org.

*Acknowledgment.* The material synthesis was supported by the U.S. Department of Energy, Office of Science, Basic Energy Sciences (BES), Materials Sciences and Engineering Division. The optical characterization, optothermal Raman measurements, theoretical calculations and analysis were performed at the Center for Nanophase Materials Sciences, which is a DOE Office of Science User Facility. The transient absorption measurement was supported by the NSF grant (DMR-

1505852). L. L. was supported by the Eugene P. Wigner Fellowship at the Oak Ridge National Laboratory (ORNL). J.Z. was supported by the "GO" program at ORNL. Part of the computations were performed using the resources of the Center for Computational Innovation at Rensselaer Polytechnic Institute.

## REFERENCES AND NOTES

1. Aharonovich, I.; Englund, D.; Toth, M. Solid-State Single Photon Emitters. *Nat. Photonics* **2016**, *10*, 631−641.
2. Lin, Z.; McCreary, A.; Briggs, N.; Subramanian, S.; Zhang, K.; Sun, Y.; Li, X.; Borys, N. J.; Yuan, H.; Fullerton-Shirey, S.; Chernikov, A.; Zhao, H.; McDonnell, S.; Lindenberg, A. M.; Xiao, K.; LeRoy, B. J.; Drndić, M.; Hwang, J. C. M.; Park, J.; Chhowalla, M.; et al. 2D Materials Advances: From Large Scale Synthesis and Controlled Heterostructures to Improved Characterization Techniques, Defects and Applications. *2D Mater*. **2016**, *3*, 042001.
3. Xia, F.; Wang, H.; Xiao, D.; Dubey, M.; Ramasubramaniam, A. Two-Dimensional Material Nanophotonics. *Nat. Photonics* **2014**, *8*, 899−907.
4. Xu, X.; Yao, W.; Xiao, D.; Heinz, T. F. Spin and Pseudospins in Layered Transition Metal Dichalcogenides. *Nat. Phys*. **2014**, *10*, 343−350.
5. Sie, E. J.; Lui, C. H.; Lee, Y. −H.; Kong, J.; Gedik, N. Large, Valley-Exclusive Bloch-Siegert Shift in Monolayer $WS_2$. *Science* **2017**, *355*, 1066−1069.
6. Mak, K. F.; He, K.; Lee, C.; Lee, G. H.; Hone, J.; Heinz, T. F.; Shan, J. Tightly Bound Trions in Monolayer $MoS_2$. *Nat. Mater.* **2013**, *12*, 207−211.
7. Low, T.; Chaves, A.; Caldwell, J. D.; Kumar, A.; Fang, N. X.; Avouris, P.; Heinz, T. F.; Guinea, F.; Martin-Moreno, L.; Koppens, F. Polaritons in Layered Two-Dimensional Materials. *Nat. Mater.* **2017**, *16*, 182−194.
8. Goli, P.; Legedza, S.; Dhar, A.; Salgado, R.; Renteria, J.; Balandin, A. A. Graphene-Enhanced Hybrid Phase Change Materials for Thermal Management of Li-Ion Batteries. *J. Power Sources* **2014**, *248*, 37−43.

9. Wang, Y.; Xu, N.; Li, D.; Zhu, J. Thermal Properties of Two Dimensional Layered Materials. *Adv. Funct. Mater.* **2017**, *27*, 1604134.

10. Seol, J. H.; Jo, I.; Moore, A. L.; Lindsay, L.; Aitken, Z. H.; Pettes, M. T.; Li, X.; Yao, Z.; Huang, R.; Broido, D.; Mingo, N.; Ruoff, R. S. Two-Dimensional Phonon Transport in Supported Graphene. *Science* **2010**, *328*, 213−216.

11. Ghosh, S.; Bao, W.; Nika, D. L.; Subrina, S.; Pokatilov, E. P.; Lau, C, N.; Balandin, A. A. Dimensional Crossover of Thermal Transport in Few-Layer Graphene. *Nat. Mater.* **2010**, *9*, 555−558.

12. Bae, M. –H.; Li, Z.; Aksamija, Z.; Martin, P. N.; Xiong, F.; Ong, Z. –Y.; Knezevic, I.; Pop, E. Ballisitc to Diffusive Crossover of Heat Flow in Graphene Ribbons. *Nat. Commun.* **2013**, *4*, 1734.

13. Xu, X.; Pereira, F.; Wang, Y.; Wu, J.; Zhang, K.; Zhao, X.; Bae, S.; Tinh Bui, C.; Xie, R.; Thong, J. T.; Hong, B.; Loh, K. P.; Donadio, D.; Li, B.; Ozyilmaz, B. Length-Dependent Thermal Conductivity in Suspended Single-Layer Graphene. *Nat. Commun.* **2014**, *5*, 3689.

14. Vuong, T. Q. P.; Liu, S.; Van der Lee, A.; Cusco, R.; Artus, L.; Michel, T.; Valvin, P.; Edgar, J. H.; Cassabois, G.; Gil, B. Isotope Engineering of van der Waals Interactions in Hexagonal Boron Nitride. *Nat. Mater.* **2018**, *17*, 152−158.

15. Cardona, M.; Thewalt, M. L. W. Isotope Effects on the Optical Spectra of Semiconductors. *Rev. Mod. Phys.* **2005**, *77*, 1173−1224.

16. Wu, Y.; Tong, Q.; Liu, G. −B.; Yu, H.; Yao, W. Spin-Valley Qubit in Nanostructures of Monolayer Semiconductors: Optical Control and Hyperfine Interaction. *Phys. Rev. B* **2016**, *93*, 045313.

17. Saeedi, K.; Simmons, S.; Salvail, J. Z.; Dluhy, P.; Riemann, H.; Abrosimov, N. V.; Becker, P.; Pohl, H. -J.; Morton, J. J. L.; Thewalt, M. L. W. Room-Temperature Quantum Bit Storage Exceeding 39 Minutes Using Ionized Donors in Silicon-28. *Science* **2013**, *342*, 830−833.

18. Itoh, K. M.; Watanabe, H. Isotope Engineering of Silicon and Diamond for Quantum Computing and Sensing Applications. *MRS Commun.* **2014**, *4*, 143−157.

19. Chen, S.; Wu, Q.; Mishra, C.; Kang, J.; Zhang, H.; Cho, K.; Cai, W.; Balandin, A. A.; Ruoff, R. S. Thermal Conductivity of Isotopically Modified Graphene. *Nat. Mater.* **2012**, *11*, 203−207.

20. Wu, X.; Yang, N.; Luo, T. Unusual Isotope Effect on Thermal Transport of Single Layer Molybdenum Disulphide. *Appl. Phys. Lett.* **2015**, *107*, 191907.

21. Balandin, A. A. Phonon Engineering in Graphene and van der Waals Materials, *MRS Bull.* **2014**, *39*, 817-823.

22. Nika, D. L.; Balandin, A. A. Two-Dimensional Phonon Transport in Graphene, *J. Phys.: Condens. Matter* **2012**, *24*, 233203.

23. Ling, X.; Lee, Y. -H.; Lin, Y.; Fang, W.; Yu, L.; Dresselhaus, M. S.; Kong, J. Role of the Seeding Promoter in $MoS_2$ Growth by Chemical Vapor Deposition. *Nano Lett.* **2014**, *14*, 464−472.

24. Li, X.; Lin, M. -W.; Lin, J.; Huang, B.; Puretzky, A. A.; Ma, C.; Wang, K.; Zhou, W.; Pantelides, S. T.; Chi, M.; Kravchenko, I.; Fowlkes, J.; Rouleau, C. M.; Geohegan, D. B.; Xiao, K. Two-Dimensional GaSe/$MoSe_2$ Misfit Bilayer Heterojunctions by van der Waals Epitaxy. *Sci. Adv.* **2016**, *2*, e1501882.

25. Liang, L.; Meunier, V. First-Principles Raman Spectra of $Mos_2$, $WS_2$ and Their Heterostructures. *Nanoscale*. **2014**, *6*, 5394−5401.

26. Lee, C.; Yan, H.; Brus, L. E.; Heinz, T. F.; Hone, J.; Ryu, S. Anomalous Lattice Vibrations of Single- and Few-Layer $MoS_2$. *ACS Nano* **2010**, *4*, 2695−2700.
27. Molina-Sánchez, A.; Wirtz, L. Phonons in Single-Layer and Few-Layer $MoS_2$ And $WS_2$. *Phys. Rev. B* **2011**, *84*, 1−8.
28. Tuschel, D. Resonance Raman and Photoluminescence Spectroscopy and Imaging of Few-Layer $MoS_2$. *Spectroscopy* **2015**, *30*, 14−29.
29. Chakraborty, B.; Matte, H. S. S. R.; Sood, A. K.; Rao, C. N. R. Layer-Dependent Resonant Raman Scattering of a Few Layer $MoS_2$. *J Raman Spectrosc*. **2013**, *44*, 92−96.
30. Cai, W.; Moore, A. L.; Zhu, Y.; Li, X.; Chen, S.; Shi, L.; Ruoff, R. S. Thermal Transport in Suspended and Supported Monolayer Graphene Grown by Chemical Vapor Deposition. *Nano Lett*. **2010**, *10*, 1645−1651.
31. Yan, R.; Simpson, J. R.; Bertolazzi, S.; Brivio, J.; Watson, M.; Wu, X.; Kis, A.; Luo, T.; Hight Walker, A. R.; Xing, H. G. Thermal Conductivity of Monolayer Molybdenum Disulfide Obtained from Temperature-Dependent Raman Spectroscopy. *ACS Nano* **2014**, *8*, 986−993.
32. Zhang, X.; Sun, D.; Li, Y.; Lee, G. -H.; Cui, X.; Chenet, D.; You, Y.; Heinz, T. F.; Hone, J. C. Measurement of Lateral and Interfacial Thermal Conductivity of Single- and Bilayer $MoS_2$ and $MoSe_2$ Using Refined Optothermal Raman Technique. *ACS Appl. Mater. Interfaces* **2015**, *7*, 25923−25929.
33. Balandin, A. A.; Ghosh, S.; Bao, W.; Calizo, I.; Teweldebrhan, D.; Miao, F.; Lau, C. N. Superior Thermal Conductivity of Single-Layer Graphene. *Nano Lett.* **2008**, *8*, 902−907.
34. Sahoo, S.; Gaur, A. P. S.; Ahmadi, M.; Guinel, M. J.−F.; Katiyar, R. S. Temperature-Dependent Raman Studies and Thermal Conductivity of Few-Layer $MoS_2$. *J. Phys. Chem. C* **2013**, *117*, 9042−9047.
35. Tamura, S. Isotope Scattering of Dispersive Phonons in Ge. *Phys. Rev. B* **1983**, *27*, 858.

36. Li, W.; Carrete, J.; Katcho, N. A.; Mingo, N. ShengBTE: A Solver of the Boltzmann Transport Equation for Phonons. *Comp. Phys. Commun.* **2014**, *185*, 1747−1758.

37. Casimir, H. B. G. Note on the Conduction of Heat in Crystals. *Physica* **1938**, *5*, 495–500.

38. Yarali, M.; Brahmi, H.; Yan, Z.; Li, X.; Xie, L.; Chen, S.; Kumar, S.; Yoon, M.; Xiao, K.; Mavrokefalos, A. The Effect of Metal Doping and Vacancies on the Thermal Conductivity of Monolayer Molybdenum Diselenide. *ACS Applied Materials & Interfaces* **2018**, *10***,** 4921–4928.

39. Zhang, H.; Lee, G.; Cho, K. Thermal Transport in Graphene and Effects of Vacancy Defects. *Phys. Rev. B* **2011**, *84*, 115460.

40. Jo, I.; Pettes, M. T.; Lindsay, L.; Ou, E.; Weathers, A.; Moore, A. L.; Yao, Z.; Shi, L. Reexamination of Basal Plane Thermal Conductivity of Suspended Graphene Samples Measured by Electro-Thermal Micro-Bridge Methods. *AIP Adv.* **2015**, *5*, 053206.

## Figures

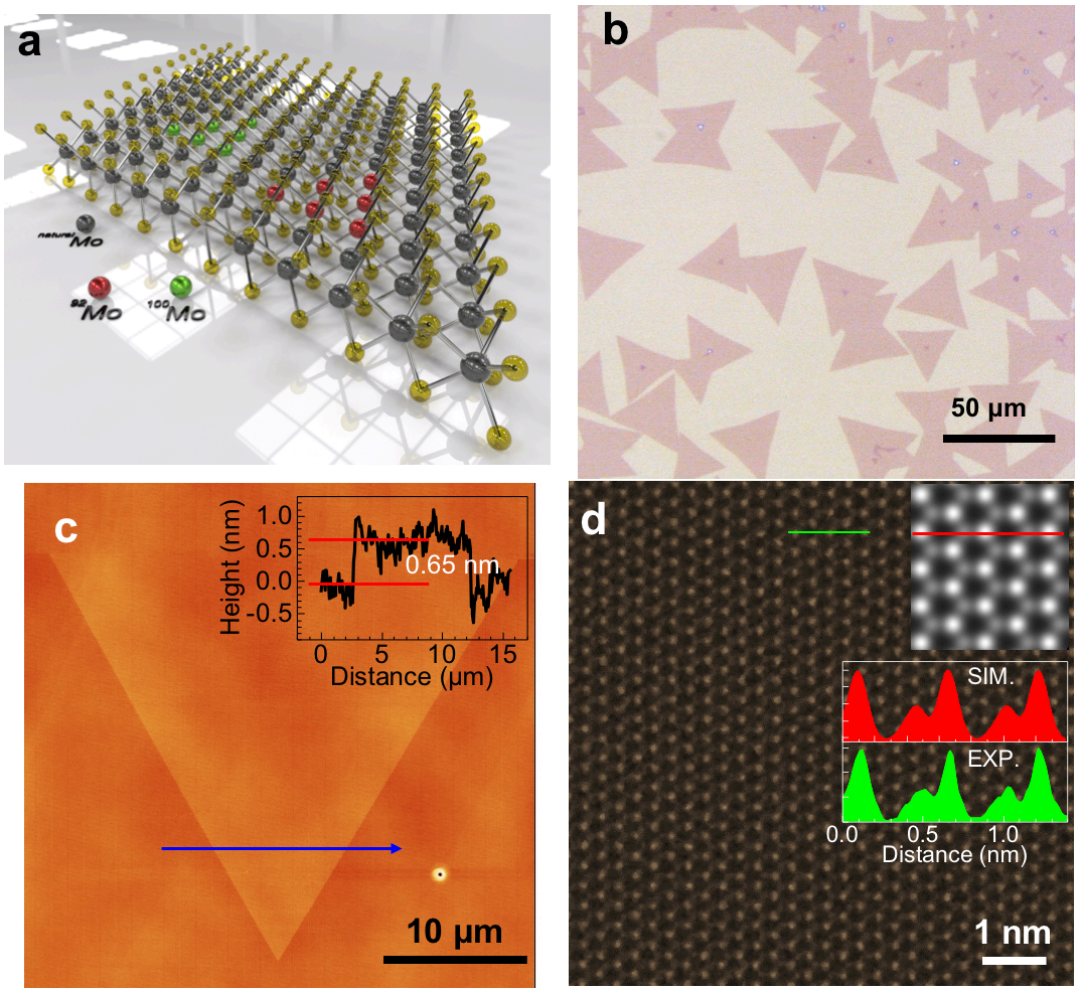


**Figure 1.** Structure of isotopically enriched $MoS_2$ monolayers. (**a**) Schematic of monolayer $MoS_2$ crystal with different Mo isotopes. (**b**) Optical micrograph of $^{100}MoS_2$ monolayers grown on a $SiO_2$ (250 nm)/Si substrate. (**c**) AFM image of a $^{100}MoS_2$ monolayer. Inset is the height profile along the blue arrow, showing a typical thickness of 0.65 nm for monolayer $MoS_2$. (**d**) ADF-STEM image showing the atomic structure of $^{100}MoS_2$ monolayer in plane view. Insets are the simulated ADF-STEM image and line profiles along the green and red lines, showing good consistence between simulated and observed atomic structure.

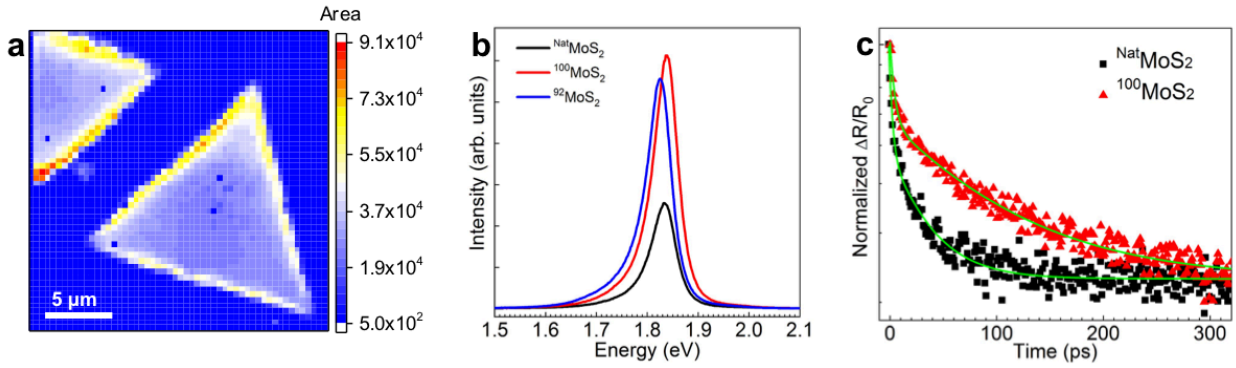


**Figure 2.** Optical and electrical properties. (**a**) PL mapping for $^{100}MoS_2$ monolayers representing PL spectra integrated from 1.6 eV (~775 nm) to 2.0 eV (~620 nm) acquired using a 532 nm laser. (**b**) PL spectra acquired from the centers of triangular monolayer crystals of $^{Nat}MoS_2$ (black curve), $^{92}MoS_2$ (blue curve), and $^{100}MoS_2$ (red curve) on $SiO_2$ substrates showing relative band shifts and intensities. (**c**) Differential reflection signal acquired from $^{Nat}MoS_2$ (black scattered dots) and $^{100}MoS_2$ (red scattered dots) monolayers with a 388 nm pump and a 670 nm probe pulse. Solid curves are bi-exponential decay fits.

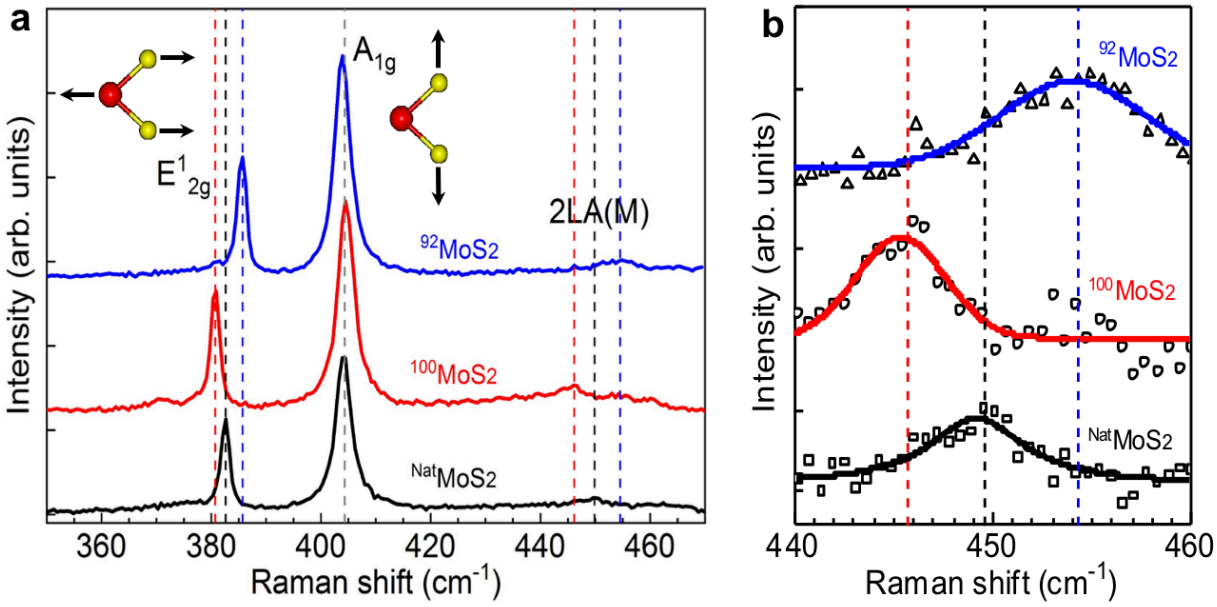


**Figure 3.** (**a**) Raman spectra of $^{Nat}MoS_2$ (black curve), $^{92}MoS_2$ (blue curve), and $^{100}MoS_2$ (red curve) monolayers acquired using a 532 nm laser. (**b**) Enlarged view of the 2LA(M) modes in the Raman spectra.

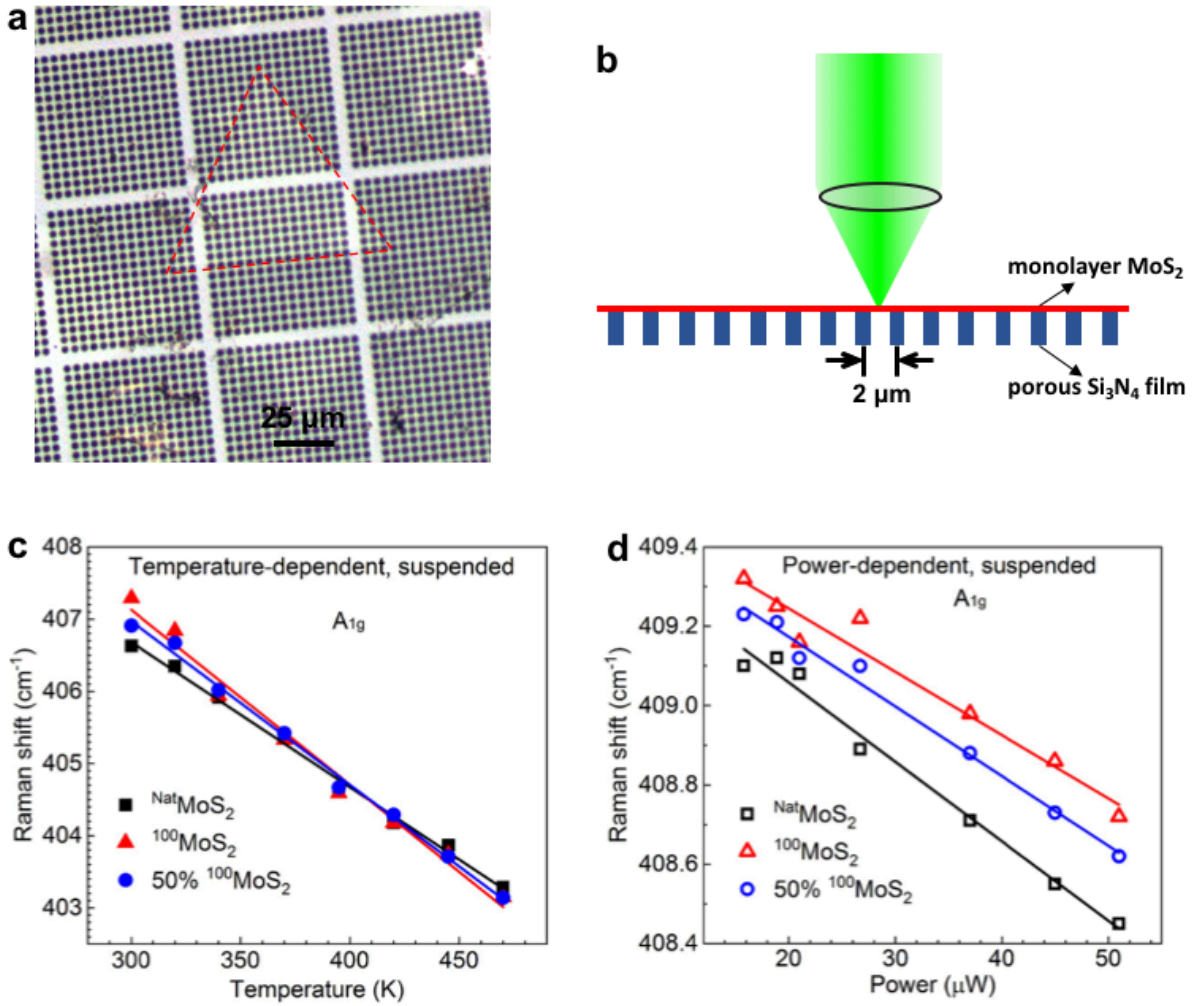


**Figure 4.** (**a**) Optical micrograph of the CVD-grown $MoS_2$ monolayers transferred on a 50 nm-thick porous $Si_3N_4$ film (~2 μm pore size) supported by a Si TEM grid. The dashed triangle highlights a triangular monolayer. (**b**) Illustration of monolayer $MoS_2$ on porous $Si_3N_4$ (with both suspended and supported regions) excited by a focused 532 nm laser for temperature and power dependent Raman measurements. (**c**) Temperature-dependent energy of $A_{1g}$ mode of suspended $^{Nat}MoS_2$ (black scattered symbols), $^{100}MoS_2$ (red scattered symbols), and 50% $^{100}MoS_2$ (blue scattered symbols) monolayers at a fixed excitation laser (532 nm) power. (**d**) Excitation laser power-dependent energy of $A_{1g}$ mode of suspended $^{Nat}MoS_2$ (black scattered symbols), $^{100}MoS_2$

(red scattered symbols), and 50% $^{100}MoS_2$ (blue scattered symbols) monolayers at room temperature. The solid curves are linear fits.

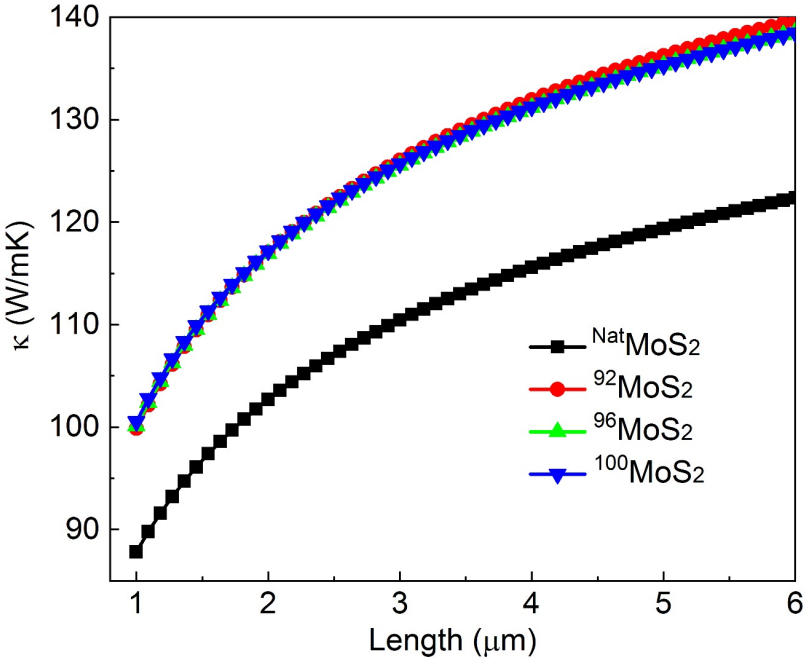


**Figure 5.** Theoretical thermal conductivity of monolayer natural and Mo-isotopically enriched $MoS_2$ as a function of sample length by first-principles calculations. The $^{92}MoS_2$, $^{96}MoS_2$, and $^{100}MoS_2$ only consider phonon-phonon scattering and boundary scattering, while $^{Nat}MoS_2$ includes extra isotope scattering.

**Table 1.** Experimental and calculated (in brackets) energies and energy shifts of Raman modes in $^{Nat}MoS_2$, $^{92}MoS_2$, and $^{100}MoS_2$ monolayers.

| *Geometry* | *Mode* | *Frequency ($cm^{-1}$)* | | | *Maximum peak shifts ($cm^{-1}$)* |
|---|---|---|---|---|---|
| | | *$^{92}MoS_2$* | *$^{Nat}MoS_2$* | *$^{100}MoS_2$* | |
| 1L | $E^1_{2g}$ | 385.7 (395.0) | 382.6 (391.6) | 380.7 (388.5) | 5.0 (6.5) |
| | $A_{1g}$ | 403.7 (411.2) | 404.2 (411.2) | 404.5 (411.2) | 0.8 (0.0) |
| | 2LA(M) | 454.5 (483.9) | 449.9 (476.5) | 446.2 (469.6) | 8.3 (14.3) |

**Table 2.** Temperature coefficient ($\chi_T$), power coefficient ($\chi_P$), thermal resistance ($R_m$), of $Si_3N_4$-supported and suspended $MoS_2$ monolayers, and the suspended thermal conductivity ($\kappa_{sus}$) of the monolayer. The theoretical suspended thermal conductivity using first-principles calculation (CAL.), as well as the values reported previously (ref. 28, 29) are also presented for comparison.

| *Materials* | $\chi_T$ ($cm^{-1}$/K) | | $\chi_P$ ($cm^{-1}$/μW) | | $R_m$ (K/μW) | | $\kappa_{sus}$ (W/mK) |
|---|---|---|---|---|---|---|---|
| | *Supported* | *Suspended* | *Supported* | *Suspended* | *Supported* | *Suspended* | |
| $^{Nat}MoS_2$ | -0.0211 ± 0.0007 | -0.0201 ± 0.0006 | -0.0056 ± 0.0002 | -0.020 ± 0.001 | 0.2654 ± 0.0007 | 0.995 ± 0.020 | 40.8 ± 0.8 |
| $^{100}MoS_2$ | -0.0184 ± 0.0006 | -0.0242 ± 0.0012 | -0.0049 ± 0.0004 | -0.016 ± 0.002 | 0.2663 ± 0.0131 | 0.661 ± 0.050 | 61.6 + 5.6/ -4.0 |
| 50% $^{100}MoS_2$ | - | -0.0227 ± 0.0006 | - | -0.0176 ± 0.0008 | - | 0.775 ± 0.035 | 52.8 ± 2.4 |
| $^{Nat}MoS_2$ (CAL.) | - | - | - | - | - | - | 87.81 |
| $^{100}MoS_2$ (CAL.) | - | - | - | - | - | - | 100.52 |
| $^{Nat}MoS_2$ [28] | - | -0.013 | -0.010 | -0.0109 | - | 0.769 | 34.5 |
| $^{Nat}MoS_2$ [29] | -0.0167 ($Au/SiO_2$-supported) | -0.0203 | -0.0204 ($Au/SiO_2$-supported) | -0.0987 | 4.862 | 1.222 | 84 |

TOC figure